applied mechanics

MDPI

Article

Path and Speed Profile Generation for Computing Chassis Loads Required for Endurance Assessment

Markus Bergold [1,*] and Dieter Bestle [2,†]

[1] Mercedes-Benz AG, Benzstr. Gate 16, 71063 Sindelfingen, Germany
[2] Engineering Mechanics and Vehicle Dynamics, Brandenburg University of Technology Cottbus-Senftenberg, Siemens-Halske-Ring 14, 03046 Cottbus, Germany; bestle@b-tu.de
* Correspondence: markus.bergold@mercedes-benz.com
† Retired.

Abstract

Endurance of automobile parts is essential since failure of safety-relevant parts enforces very expensive recall campaigns and damages the reputation of the respective car manufacturer. Therefore, endurance assessment is an important sub-task within the design process, and extensive physical tests of components, parts and even the full vehicle are performed based on either simulated load data or measured loads during test drives on public roads. The latter, however, is only available after the existence of first prototypes, whereas the former would reduce development time of vehicles dramatically by shifting important conceptual decisions to the early digital development phase. During real tests on roads, the test driver would select speed and path, whereas for full-vehicle simulation these time functions need to be generated based on road data and vehicle performance data. In order to investigate the influence of vehicle control on endurance assessment, three idealized paths within the road borders are defined and generated: the lane center line, the rightmost lane along to the right lane border, and a time-optimal trajectory determined by solving a simplified optimal control problem. Speed specifications account for legal, curvature-related and vehicle-specific limits. These functions then serve as the basis of a full-vehicle simulation, where the car is represented by a multi-body system model including a driving controller to regulate the speed and follow the selected path like a real-world driver. The approach is validated by applications to a generic road section and a measured country road, where significant differences in the resulting longitudinal and lateral wheel loads can be observed by just modifying the path and the linked velocity profile. While lateral loads are comparable for different trajectories, longitudinal loads determined along the time-optimal path are 12% lower than those for the other two trajectories.

Keywords: chassis loads; velocity profile; trajectory planning; minimum lap time problem; Simpack driver model

Check for updates

Received: 14 September 2026
Revised: 19 October 2026
Accepted: 3 November 2026
Published: 6 November 2026

Copyright: © 2026 by the authors. Licensee MDPI, Basel, Switzerland. This article is an open access article distributed under the terms and conditions of the Creative Commons Attribution (CC BY) license.

1. Introduction

To meet the increasing demand for accelerating the development of new passenger cars, manufacturers tend to shift important design decisions to the beginning of product development by replacing real-world experiments with simulations step by step. A further advantage of making decisions as early as possible is the reduction in late and thus expensive problem findings during the hardware phase or even if the car is with the customer already. One of the problems that most severely damages a manufacturer's reputation,

and must therefore be avoided in practice, is component failure. A customer expects a reliable car over the whole lifecycle, which is why components have to undergo multiple experiments and fatigue tests to meet the expected loads. Braess [1] points out that all products placed on the market must meet product safety requirements clearly defined by European and German legal regulations, claiming that all products shall only be placed on the market if its intended or reasonably foreseeable use does not pose any risk to human health or safety [2]. While load assumptions in ship, train and aircraft design are specified by regulations, standards and law, no such regulations exist for road vehicles [3]. Therefore, every manufacturer has to define a proper load spectrum by itself, where, according to Köhler [3], an industrial endurance standard of 300,000 km has been established. To ensure this, a major task in the early design process is the determination of expected loads.

Making correct load assumptions is rather challenging. To model customer behavior, various approaches may be found in the literature which range from surveys on customer usage behavior [4–6] to reading measurement data from specially equipped customer vehicles [7] and recording CAN data from real customer drives with cars [8] or motorcycles [9,10]. These datasets are helpful in terms of vehicle usage in the field, but provide only indirect information about the loads acting on chassis components. Just taking such data from predecessor series is also insufficient, since it may deviate from those acting on the new car to be developed. Especailly, if forces acting on bushings or struts have to be determined, additional simulations and computations are inevitable.

Sonsino [11] differentiates between service loads, special events and misuse events. The latter, such as sliding on icy roads towards a curbstone, should not occur during the lifecycle of a car. Despite the uncertainty of occurrence of such loads, it has to be ensured that wheel-carrying components prevent wheel detachment by using sufficiently ductile material. Special events may happen several times in a car's lifecycle. Such incidents include, for example, striking an obstacle slowly or moving off on slippery roads. Most interesting are service loads, which appear numerous times during intended use cases of the car including cornering, acceleration and braking, as well as from roughness of the street surface.

While special and misuse events are short-lived and can be tested and validated rather quickly, service loads are by definition long-lasting signals. In order to test chassis components efficiently, manufacturers usually contract the testing signal by increasing the amplitude and frequency of customer-relevant loads being measured while driving prototype cars on test tracks and proving grounds with a very rough surface [5]. But only structural components made of aluminum or steel may be exposed to contracted signals without disturbing endurance assessment [12]. Functional components like rubber bushings must not undergo a test signal with higher amplitude and frequency than customer-related loads; otherwise, the bushings may heat up, the rubber may devulcanize and so-called phantom damages arise [13].

Determination of correct loads for functional components requires the generation of customer-oriented load profiles in real-time. For this purpose, Mercedes-Benz actually drives along a so-called "customer route" which follows public roads and consists of representative portions of city, highway, country road, parking garage, and rough road sections. Such an entire route is shown in Figure 1.

The customer route has a total length of approximately 150 km and is driven with prototypes or major assembly carriers. The test drives are conducted in accordance with German traffic regulations by professional test drivers attempting to represent the 99% customer, as long as traffic conditions permit. This means that the driving style aims to cover 99% of all customers in terms of acceleration and deceleration behavior as well as lateral acceleration in curves depending on the chosen track. Based on these measurements, time

sequences are extrapolated to achieve the desired mileage of a car over its whole lifecycle. From these sequences, load collectives are assembled, which are then used to design and ultimately secure the functional components. However, such an approach is only applicable after real prototypes are built to conduct the test drives. Consequently, the loads acting on functional components can only be determined once important decisions in design and concept have already been made.

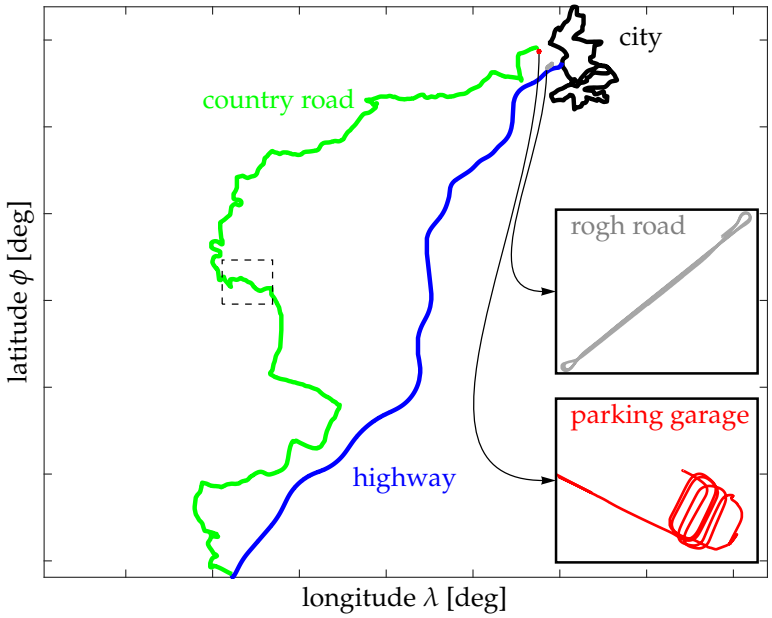


Figure 1. The customer route of Mercedes-Benz showing five parts related to city, highway, country road, parking garage and rough road by different colors in GPS coordinates; the dashed square labels a piece of the country road being simulated later in this work.

To circumvent this disadvantage, simulations may be utilized to predict loads before a first physical prototype is built. Therefore, the whole, actually experiment-based and well-established industrial process of selecting a load case, setting up a prototype vehicle, driving on public roads to record measurements, evaluation of load data by counting algorithms [3,14] and derivation of load sets for component design needs to be transferred into the virtual world by replacing the real prototype vehicle and the test driver with simulation models. For simulation, various methods may be applied; however, according to Duni [15] and Hu [16], some strategies result in insufficient quality and/or long computation times. Utilization of multi-body system (MBS) models used by Lieven [17], Schmeitz [18], Weber [19], Pawar [20] and Brandes [21] allow to perform full-vehicle simulation with detailed chassis models in reasonable time. Depending on specific foci, the classical rigid-body approach may be extended by flexible elements like elastic car bodies [17] or detailed tire models for rough road simulations [19,20]. For simulation on normal roads and handling courses, however, a single contact point per wheel in combination with the magic formula tire model by Pacejka [22] is often sufficient.

To ensure that the model will drive along a specified track, the model needs to include a driver model following a pre-defined reference trajectory and speed profile. Both specifications may come either from previously conducted measurements with the same vehicle being later simulated [19,21] or need to be determined such that they are representative of 99% of drivers. Replicating a real driver in simulations has been a big challenge for decades [23]. Besides academic surveys [24], most of the industrial simulations use proprietary driver models either developed by the companies themselves [21] or provided by commercial MBS software suppliers [25]. Typically, these controllers require a reference

trajectory with corresponding speed, to then conduct simulations for parameter studies independently of varying traffic conditions or any undesired traffic scenarios such as traffic jams.

Real virtual prototyping has to avoid any a priori measurements, but has to find a proper reference track, which accounts for the actual vehicle properties. While human test-drivers will choose from an infinite set of trajectories and corresponding velocities in the actual driving situation, a unique representative trajectory has to be defined for simulation. In order to make a proper choice that mimics the 99% driver, it is important to first investigate the impact of the chosen path and associated velocity profile on chassis loads. Therefore, speed profile generation and trajectory planning for public roads such as the customer route of Mercedes-Benz is a special focus of the present paper. According to the historical survey by Massaro [26], various strategies with different complexity have been developed for trajectory planning for automotive and motorcycle racing, where the major objective of most strategies is to minimize the lap time while meeting constraints regarding track boundaries and vehicle capabilities. However, in recent years, research on autonomous driving has set new requirements for trajectory planning, seeking maximum comfort, avoidance of obstacles and meeting safety issues [27]. Also, special cases like optimal speed control for lane change [28] or control strategies for maintaining lanes [29] have been considered. Although these developments do not directly apply to the focus of the actual paper, which is not racing but driving on public roads, such strategies may apply to drivers in a hurry who cut tight corners resulting in tracks similar to those observed in Formula One races. Therefore, path planning algorithms may also apply here, which is why a concept similar to the one described in [30] is applied for defining such kinds of paths. It uses a simple bicycle vehicle model on a 2D road in combination with Pacejka's tire formula [22] and quasi-static vertical load distribution.

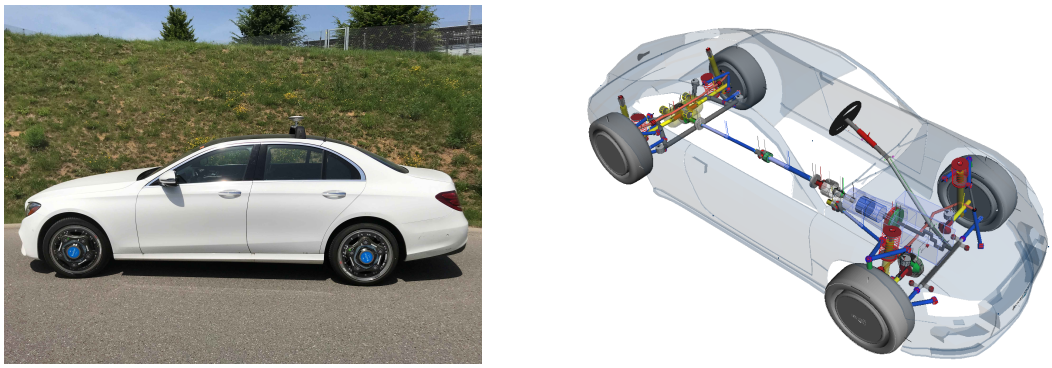
Section 2 introduces an established MBS model used for full-vehicle simulation to estimate realistic loads. Part of the model is a commercial driving controller where some pre-investigations with idealized maneuvers are performed to properly set the control parameters. Since drive control requires a pre-defined path and speed, Section 3 describes the determination of a proper speed profile based on the legally maximum permissible speed, road curvature and the longitudinal acceleration properties of the vehicle to be designed. The route necessary for maintaining the road and for speed profile generation is determined in Section 4, where three idealized trajectories are generated considering road boundaries: the lane center, a rightmost track, and a time-optimal trajectory. In the subsequent Section 5, the influence of these different paths and speed profiles on the loads in the chassis is investigated. The partly unexpected results, demonstrating the importance of the reported investigations, are summarized in Section 6.

2. Vehicle Simulation Using Multi-Body System Model

Since the simulation is intended to cover typical driving on public roads and the determination of the loads that occur during such driving, multi-body simulation is used to model virtual vehicles. The multi-body system method is particularly well-suited for calculating the motion behavior of systems with large body movements. Thereby, the system to be simulated is represented by a finite number of rigid bodies, which are connected by massless joints and force elements. Force elements include springs, dampers, friction elements and actuators. The equations of motion are derived from momentum and angular momentum equations. The resulting ordinary differential equations are here set up and solved using Simpack 2022x.5, a commercial multi-body simulation software package [25]. A detailed description of the theory of MBS simulation may be found, e.g., in [31].

Multi-body system models have the advantage over field tests that vehicle investigations can be performed already in early design stages without the need for expensive physical prototypes. Further, chassis internal loads can be determined much more easily than with measurements requiring the application of respective sensors. Since the behavior of individual bodies is calculated separately, loads acting on them can be determined directly. These loads can then be used in subsequent processes, such as strength analysis and determination of fatigue behavior of components.

The chosen MBS model shown in Figure 2b simulates a predecessor model of the current E-class limousine from Mercedes-Benz (internal designation BR213, see Figure 2a). The model consists of several rigid bodies representing the four-link front axles and the five-link rear axles, and a single rigid body representing the vehicle body. The steering torsion bar is modeled as an Euler–Bernoulli beam. The vehicle has a passive suspension with steel springs and conventional dampers. The tire forces and moments depending on vertical excitation and slip are calculated using the Pacejka tire model [22]. Its parameters are derived from measurements of the tire on a test rig. Bearing stiffnesses are modeled using frequency-dependent characteristic curves. The drivetrain consists of engine, four-wheel drive, transmission with prop shafts, axle drives and side shafts. The engine and gearbox are not modeled in detail but represented by their total masses and moments of inertia, as well as a drive torque derived from the engine map. The transmission is represented by characteristic shift curves along with the respective gear ratios.



(**a**) (**b**)

Figure 2. Mercedes-Benz E-class car of the model series BR213 (**a**) and corresponding MBS-model containing chassis, drivetrain and vehicle body (**b**).

The whole MBS model consists of more than 170 rigid bodies, which results in nearly 260 degrees of freedom. For simplicity, the road surface is assumed to be flat. To conduct a full-system simulation, the vehicle model has to be driven along a given road (see Figure 1) with a predetermined velocity profile. A driver model is used to mimic a real test driver, maintaining the lane and adhering to the given speed. In particular, the "Simpack Driver" model is used to control the car by steering the front axle and acting on the throttle and brakes. According to the Dassault Systems manual [25], the longitudinal control part may be sketched as shown in Figure 3. It regulates the speed according to a target velocity specified as a reference value. It uses a PI-controller combined with a first-order delay. The normalized pedal position (accelerator and brake pedal) serves as control variable for the vehicle model, including the engine map.

While the longitudinal or cruise control maintains the set speed, the lateral controller maintains the specified trajectory. Despite the mutual reaction between longitudinal and lateral movements in cars, both controls are handled independently from each other in Simpack. The lateral control consists of three parts [25]:

- Yaw feedforward control based on an internal single-track model;

- Yaw feedback control based on a PI-controller;
- Lateral feedback control based on a PD controller.

The virtual lateral driver is fed with x- and y-coordinates describing the track. The output of the controller is the steering wheel angle, which is directly applied to the MBS model. As the lateral controller is not as transparent as the longitudinal part [25], some basic investigations are executed with two generic trajectories in order to analyze the behavior of the driver controller and find proper parameter settings. The first test signal is a lateral offset of $\Delta y = 0.05\,\mathrm{m}$ shown in Figure 4a, which simulates a lane change maneuver. The second test signal is the bend in Figure 4b with $\Delta\psi = 1°$, which simulates a sudden change in direction. Since initial investigations revealed some difficulties with abrupt transitions, the transitions are smoothed by the two functional sections $y_2(x)$ shown in Figure 4.

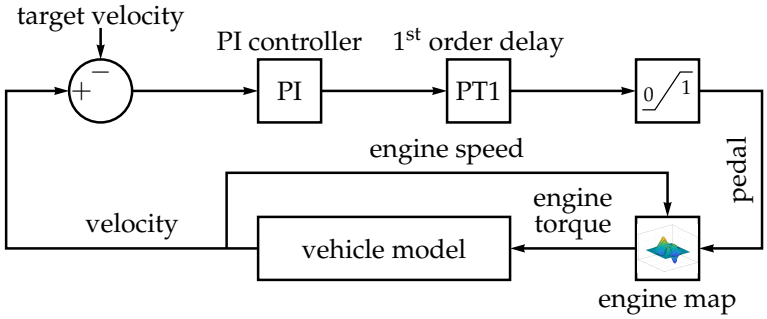
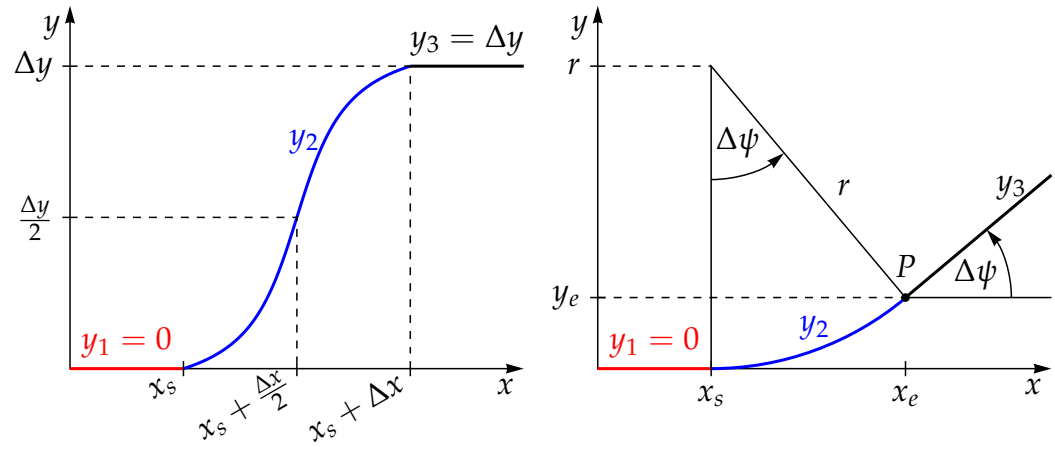


Figure 3. Structure of the longitudinal controller.



(**a**) (**b**)

Figure 4. Test functions for analyzing the lateral part of the Simpack Driver: arcus-tangens function modeling a lateral offset (**a**) and circular arc representing a bend (**b**).

Both test functions consist of three parts, respectively: (i) an initial part $y_1 \equiv 0$ to let the vehicle settle down to an equilibrium state, (ii) a transition part $y_2(x)$, and (iii) a final straight part y_3. Discontinuities take place at $x_s = 400\,\mathrm{m}$ after the initial straight part and at the end of the transition. An arcus-tangens function is used to describe the offset in Figure 4a by

$$y_2(x) = \frac{\Delta y}{2} + a \arctan\left(c\left(x - x_s - \frac{\Delta x}{2}\right)\right) \quad , \tag{1}$$

where coefficient c and distance Δx determine the sharpness of the transition. The amplitude a results from the transition condition $\Delta y = \Delta y/2 + a \arctan(c\,\Delta x/2)$ as

$$a = \frac{\Delta y}{2 \arctan(c\,\Delta x/2)} \quad . \tag{2}$$

The free parameters are chosen as $\Delta x = 100\,\mathrm{m}$ and $c = 4/\mathrm{m}$.

The transition $y_2(x)$ in Figure 4b is a circular arc given as $(x - x_s)^2 + (r - y_2)^2 = r^2$, which results in

$$y_2(x) = r - \sqrt{r^2 - (x - x_s)^2} \quad . \tag{3}$$

The radius is chosen as $r = 20\,\mathrm{m}$, covered by the turning radius of the vehicle. In the end point $x_e = x_s + r\,\sin\Delta\psi$, $y_e = r(1 - \cos\Delta\psi)$, the arc merges into a straight line

$$y_3(x) = y_e + (x - x_e)\,\tan\Delta\psi \quad . \tag{4}$$

While driving at constant velocities $v \in \{5, 15, 25\}\,\mathrm{m/s}$, the Simpack Driver is fed with x- and y-coordinates calculated from the offset and the bend. Main parameters for the lateral control of the driver model are varied to study their effect, where the "yaw driver response frequency" ω_y and the "lateral driver response frequency" ω_ψ are identified as those controller parameters with the largest impact on the responding and oscillating behavior of the vehicle. Simpack provides a manual as well as an automatic parametrization of these two frequencies. The latter, in Simpack called "online" parametrization, is calculated internally in Simpack during runtime depending on the speed and cannot be predefined. However, because this online parametrization does not add any value to the test functions here, the mentioned frequencies are set manually to constant values and studied for a wide range of values. Another parameter is the driver corridor, where no steering corrections are applied while the vehicle model remains within its bounds. To react to any trajectory deviation for maximum driver responsiveness, the corridor width is set to zero. For evaluating the controller behavior, three outputs are selected that describe the vehicle's motion and directional stability: (i) the lateral offset y, (ii) the absolute yaw angle ψ, and (iii) the steering wheel angle δ. Figure 5 shows the variation in these quantities for a selected set of frequency parameters and three different vehicle speeds.

The lateral deviation y and yaw angle ψ in Figure 5a,b show reactions of the controller already at road position $s \approx 350\,\mathrm{m}$ in advance of the upcoming discontinuity at $x_s = 400\,\mathrm{m}$. Yaw angle ψ and steering wheel angle δ in Figure 5b,c have the tendency of increasing oscillation with increasing speed which cannot be reduced without negative effect on the course at low speeds. For change of lane direction in Figure 5d–f, the yaw angle finally settles down to the bend angle of the road, where here also the oscillation frequency increases with speed. Obviously, the controller has greater difficulty adjusting the correct steering wheel angle when passing the bend than with the lateral offset.

The graphs in Figure 5 are computed using default values for lateral and yaw driver response frequencies, i.e., $\omega_y = 2.5\,\mathrm{rad/s}$ and $\omega_\psi = 6.0\,\mathrm{rad/s}$. As these values yield oscillations especially in the yaw and steering wheel angle, a full-factorial search for better parameter settings is performed using 21 equally distributed lateral frequencies ($\omega_y \in \{1, 1.5, 2, \ldots, 11\}\,\mathrm{rad/s}$) and 13 yaw frequencies ($\omega_\psi \in \{4, 5.5, \ldots, 22\}\,\mathrm{rad/s}$), which results in 273 variants. As their assessment cannot be accomplished by visually comparing the graphs as shown in Figure 5, an analytical assessment is required. Therefore, the integral error between the requirement (dashed lines in Figure 5) and the vehicle motion is calculated as

$$A^{(\eta)}_{err,\xi}(v) = \int_{t_1}^{t_2} |\Delta\,\xi|\,dt \quad \text{with} \quad \xi \in \{y, \psi, \delta\}\,, \quad \eta \in \{o, b\} \tag{5}$$

for offset (o) and bend (b), where the initial part $s < x_s$ of the traveled distance is ignored. The defective area $A^{(\eta)}_{err,\xi}$ is calculated for six different velocities $v \in \{5, 10, \ldots, 30\}$, the three relevant channels already observed in Figure 5, and the 273 parameter sets, respectively. To make these nearly 5000 values comparable, the defective areas for the three relevant

channels are weighted by $w_y = 0.617$, $w_\psi = 0.187$, $w_\delta = 0.195$ and logarithmized to reduce the magnitude of very large errors, thereby improving comparability in the representation of small errors:

$$\varepsilon^{(\eta)}(v) = \log_{10}\left(\frac{\sum_\xi w_\xi \, A^{(\eta)}_{err,\xi}(v)}{\sum_\xi w_\xi}\right) \quad . \tag{6}$$

The errors $\varepsilon^{(o)}$ for lateral offset and $\varepsilon^{(b)}$ for bend are combined as $\varepsilon(v) = w^{(o)}\,\varepsilon^{(o)}(v) + w^{(b)}\,\varepsilon^{(b)}(v)$ with further weighting factors $w^{(o)} = 0.6$ and $w^{(b)} = 0.4$, respectively, and visualized in Figure 6.

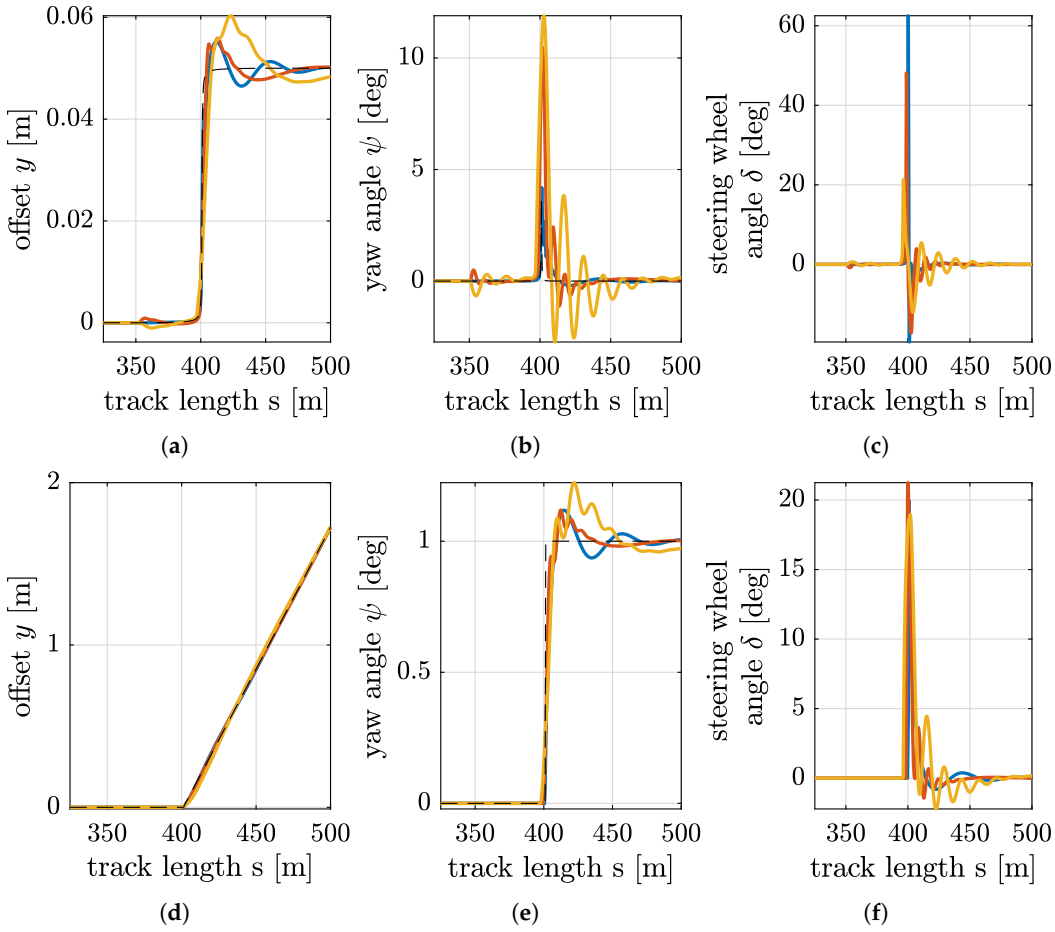


Figure 5. Behavior of the lateral Simpack controller responding to a given (– –) lateral step (**a**–**c**) and a bend (**d**–**f**) for velocities 5 m/s (—), 15 m/s (—) and 25 m/s (—).

As observed in Figure 6, with increasing velocity the region of low errors gets tighter, which would require a velocity-dependent parametrization. Since parameters cannot be changed manually during simulation in Simpack, one global parameter setup for lateral and yaw driver response frequency for all velocities is aspired to. Therefore, the six weighted deviations in Figure 6 are added together and the resulting global minimum error is found for $\omega_\psi = 10\,\mathrm{rad/s}$, $\omega_y = 3\,\mathrm{rad/s}$. This setup is used for all following simulations solved with the implicit multi-step integration scheme SODASRT2 [25] using variable step sizes and error control.

Simulations in this paper are performed on Windows servers equipped with a third-generation Intel Xeon Gold processor operating at a CPU clock rate of 3.1 GHz. For standard road drives, a real-time factor of approximately 10 is achieved, which means that one simulated second requires 10 s of computation time. In case of high vertical excitation, e.g.,

when passing a rough or paved road not considered in this paper, the real-time factor can rise up to 20 due to more iteration steps for meeting the admissible integration tolerance.

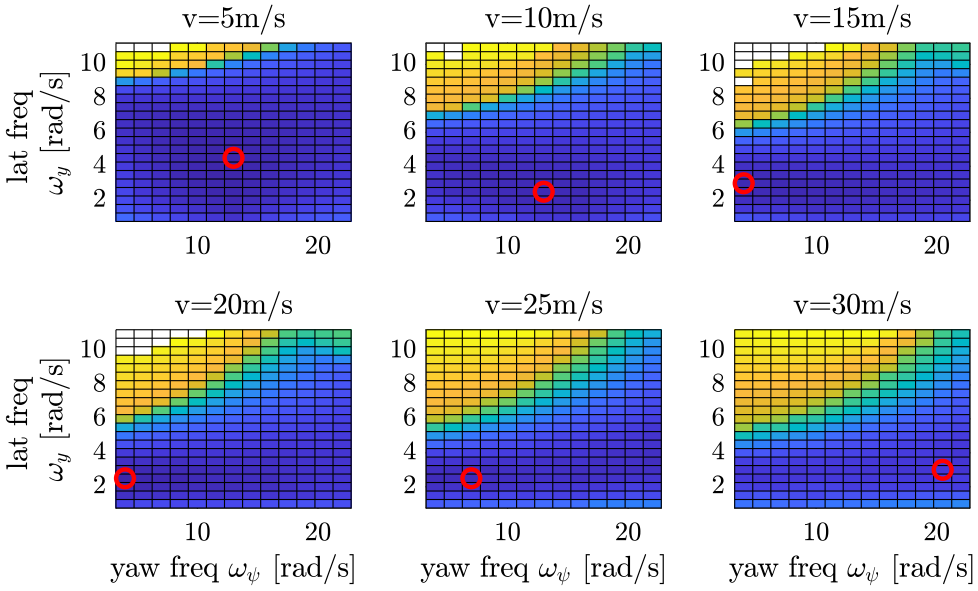


Figure 6. Weighted deviation (from small ▬ to large error ε ▬) and local minimum ○ for different velocities depending on yaw frequency ω_ψ and lateral driver frequency ω_y.

3. Determination of a Realistic Velocity Profile

The simulation of driving along a predefined road requires a velocity profile matching the road layout. The velocity profile $v(s)$ specifies the target speed for the driver controller and is determined offline ahead of the actual MBS simulation. Providing it as a function of traveled distance s has the advantage of accounting for events like speed limits linked to the route instead of time span. The influence of traffic is not considered in this work; only the following speed limits are considered:

- Legal limits $v_{lgl}(s)$ specify the maximum permissible speed, e.g., inside towns or on country roads. This information is derived from map data, e.g., by HERE via the ADASISv3 interface [32,33].
- A special case of legal speed limits are regulations at intersections, like right-of-way rules or STOP signs. Especially the latter force the driver to come to a standstill at a given position. Requirements, such as STOP signs, are marked with v_{sgn}.
- Curvature-dependent limits $v_{crv}(s)$ are mainly determined by the dynamic properties of the vehicle in curves, driving style and comfort desire. By prescribing an admissible lateral acceleration $\hat{a}_y$, the maximum possible velocity resulting from curvature $\kappa = 1/R$ of the vehicle path and the acceleration relationship $a_y = v^2/R$ is

$$v_{crv}(s) = \sqrt{\left|\frac{\hat{a}_y}{\kappa(s)}\right|} \quad .$$

  The curvature-dependent limit is required additionally to legal limits, since the latter do not cover local road geometry like narrow turns in cities or on rural roads where traffic signs would be misleading.
- Additional longitudinal dynamic velocity limits result from the vehicle's deceleration ($\hat{a}_B$ depending on brakes) and acceleration potential ($\hat{a}_D$ depending on powertrain), but mainly from the driving style. It determines how fast a transition between two speed levels can be performed.

The velocity specifications mentioned above are shown exemplarily in Figure 7 for a generic route example consisting of a straight track followed by a slight curve, where the signs are according to German traffic regulations. An initial phase with speed limit 50 km/h is followed by a 30 km/h zone. Within this zone, a STOP sign forces the driver to stop his car. A subsequent speed limit of 70 km/h is followed by an end of all restrictions, which on German country roads implies a maximum speed of 100 km/h. The following curve is modeled using two clothoids to change the curvature linearly from $\kappa = 0$ to a road part with constant radius $R = 63.66\,\mathrm{m}$ associated with $\kappa = 0.0157\,\mathrm{m}^{-1}$ and back to zero curvature as displayed in Figure 7b. Clothoids are utilized in road construction to ensure a smooth change in the car's lateral acceleration, which makes passing curves more comfortable [34]. Legal limits and the lateral dynamic limit are determined independently of each other and shown in Figure 7c by blue and orange lines, respectively. The dashed envelope defines the speed-frame

$$v_{frm}(s) = \min\Big(v_{lgl}(s), v_{crv}(s), v_{sgn}(s)\Big) \quad . \tag{7}$$

While the route is given in x- and y-coordinates, the last two charts are plotted against the traveled distance s.

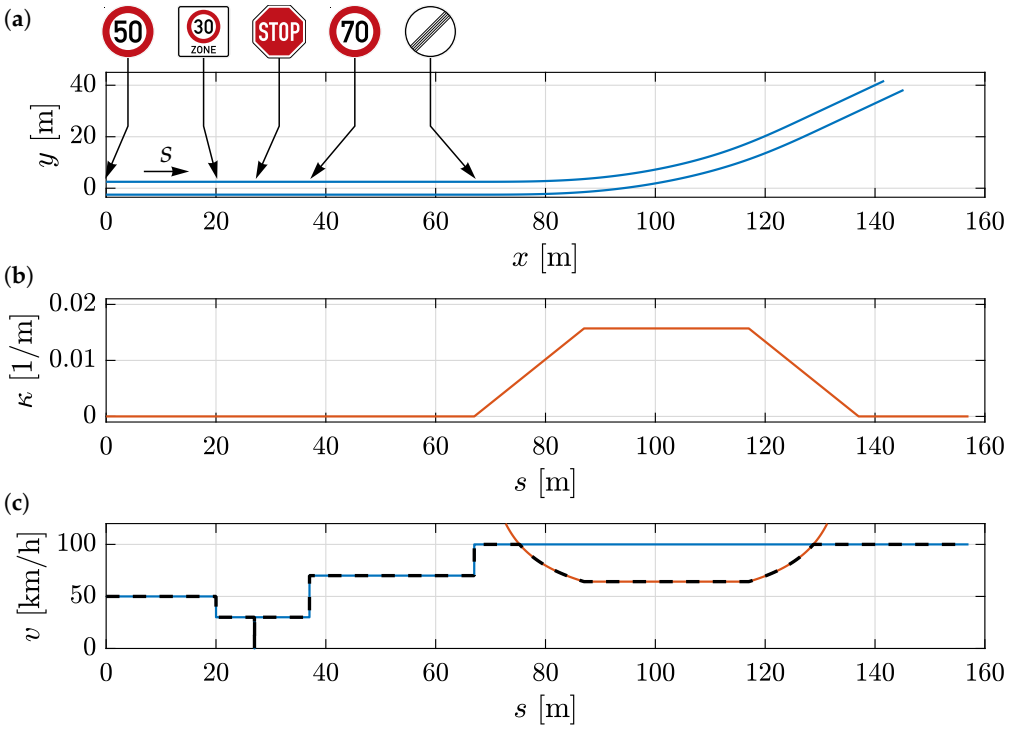


Figure 7. Generic track (—) with speed limits (**a**) and the corresponding curvature (—) (**b**) defining speed-frame $v_{frm}(s)$ (– –) as the minimum of legal velocity including sign restrictions (—) and curvature velocity (—) (**c**).

Direct application of Equation (7) causes sharp steps and kinks in the speed-frame v_{frm} as shown in Figure 7c. These discontinuities result in infinite and thus unrealistic jerks, which cannot be met with the longitudinal driver controller of Simpack. To enable a soft transition between different speed levels, the following smoothing algorithm is proposed. Generally, acceleration a is defined as the derivative of speed v with respect to time t, i.e.,

$a = dv/dt$. Since velocity is here defined as a function of track coordinate s, a conversion is necessary based on the relation

$$a = \frac{dv}{dt} \equiv \frac{dv}{ds}\frac{ds}{dt} = \frac{dv}{ds}\,v \quad \rightarrow \quad a\,ds = v\,dv \quad . \tag{8}$$

For conversion to a discrete form, we assume a constant longitudinal acceleration $a = a_{x,i}$ between two consecutive data points s_i and s_{i+1} separated by a distance $\Delta s_i = s_{i+1} - s_i$. Integration of Equation (8) then yields

$$\int_{s_i}^{s_{i+1}} a_{x,i}\,ds = \int_{v_i}^{v_{i+1}} v\,dv \quad \rightarrow \quad a_{x,i}\,(s_{i+1} - s_i) \equiv a_{x,i}\,\Delta s_i = \frac{v_{i+1}^2 - v_i^2}{2} \quad . \tag{9}$$

Applied to the speed-frame velocity, a theoretically necessary acceleration $\tilde{a}_{x,i}$ may be determined from Equation (9), which performs a transition from actual frame velocity $v_{frm,i}$ to a desired frame velocity $v_{frm,i+1}$. For smoothing, it has to be limited by the admissible longitudinal acceleration

$$\hat{a}_x := \begin{cases} \hat{a}_D & \text{for } \tilde{a}_{x,i} \geq 0 \\ \hat{a}_B & \text{for } \tilde{a}_{x,i} < 0 \end{cases} \tag{10}$$

determined by vehicle and driver characteristics, which results in an actual acceleration $a_{x,i}$. This bounded longitudinal acceleration is finally used to calculate the achievable next velocity $v_{frm,i+1}$ step by step, which overwrites the desired frame velocity. In detail, the steps resulting from Equations (9) and (10) are as follows:

$$\text{for } i = 1, 2, \ldots, n-1: \quad \tilde{a}_{x,i} = \frac{v_{frm,i+1}^2 - v_{frm,i}^2}{2\,\Delta s_i} \tag{11}$$

$$a_{x,i} = \min\{|\tilde{a}_{x,i}|, \hat{a}_x\} \cdot \operatorname{sign}(\tilde{a}_{x,i}) \tag{12}$$

$$v_{frm,i+1} := \sqrt{v_{frm,i}^2 + 2\,a_{x,i}\,\Delta s_i} \quad . \tag{13}$$

Figure 8 shows the application of this procedure to a double step velocity change containing sudden acceleration and braking maneuvers. The orange dashed curve illustrates that the velocity ramp starting at $s = 20\,\text{m}$ is determined by the chosen limit $\hat{a}_x = 5\,\text{m/s}^2$ as desired, but the deceleration ramp starting at $s = 70\,\text{m}$ is too late because it exceeds the desired black-dashed frame velocity v_{frm}, which in real-world terms would mean that a driver, passing an associated speed limit of 20 km/h at $s = 70\,\text{m}$ without prior notice, would exceed the legal velocity till $s = 86\,\text{m}$.

To prevent the issue of late braking, a case distinction must be made by treating acceleration and braking differently: while for acceleration (i.e., $\tilde{a}_{x,i} \geq 0$) the above procedure applies without restrictions, for deceleration (i.e., $\tilde{a}_{x,i} < 0$) the upper algorithm is executed in reverse direction using the velocity update

$$v_{frm,i} := \sqrt{v_{frm,i+1}^2 - 2\,a_{x,i}\,\Delta s_i} \quad , \quad i = n-1, \ldots, 2, 1\,. \tag{14}$$

After updating the speed-frame velocity step by step in both directions, the yellow curve in Figure 8 shows the improved result, where now the velocity never exceeds the prescribed frame velocity.

Several multi-body simulation studies have shown that application of a low-pass filter yields more realistic load behavior by smoothing the jerk that occurs at the beginning and the end of each speed ramp. The filter implemented here is a first-order low-pass

filter based on an exponential discretization of the continuous-time system with cutoff frequency f_g:

$$v_i := \varrho\, v_{i-1} + (1-\varrho)\, v_i \quad \text{where} \quad \varrho = e^{-2\pi f_g \Delta t} \quad . \tag{15}$$

To avoid a smoothing out of desired singularities at standstill conditions, the smoothing is performed piecewise, where each segment from one standstill to the next is treated separately. Since better filtering behavior is achieved when velocity is filtered as a function of time rather than distance, the velocity is first expressed over time, then filtered according to Equation (15), and finally mapped back as a function of the travel distance. To eliminate phase distortion, the filter is applied in both forward and backward directions, resulting in a zero-phase filtering characteristic. In order to suppress boundary artifacts, the signal is symmetrically extended prior to filtering, and afterward the extended regions are discarded to obtain a smoothed signal without phase shift or transient edge effects. Application of the described ramping algorithm for acceleration/deceleration (yellow) together with the low-pass filter to the velocity profile introduced in Figure 7 yields the velocity profile (red) shown in Figure 9.

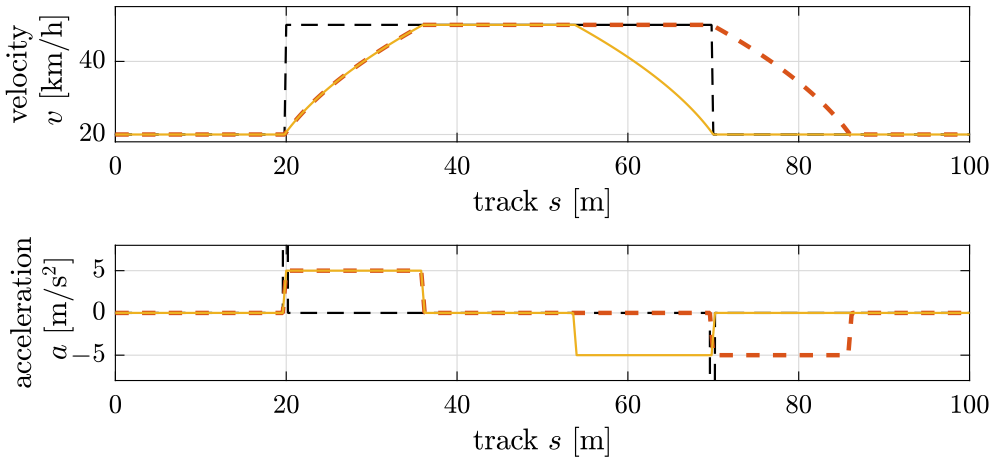


Figure 8. Ramping algorithm applied to a step-like frame velocity (▬ ▬) using only forward (▬ ▬) and forward/backward calculation (▬).

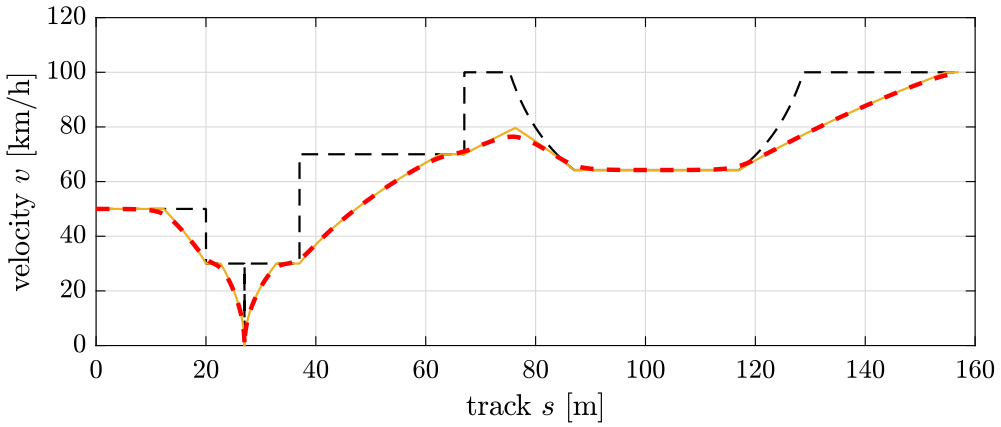


Figure 9. Based on a given speed-frame $v_{frm}(s)$ (▬ ▬), acceleration limitation (▬) and low-pass filtering (▬ ▬) are applied.

4. Idealized Travel Paths and Time-Optimal Trajectory

As stated in Section 2, a reference trajectory needs to be calculated in advance before executing the Simpack simulation. It is the reference for the Simpack Driver to control the steering angle such that the vehicle model meets the lane boundaries of the road. As

the lane width w_L is wider than the vehicle width w_V, there is an infinite possibility of trajectories within the right roadside and the lane separator on the left. In this section, three different reference trajectories are developed, cf. Figure 10:

(I) Trajectory $\mathbf{p}_{T,M}$ runs exactly in the middle between left and right lane boundaries;
(II) Trajectory $\mathbf{p}_{T,R}$ runs as far to the right as possible, taking into account the vehicle width;
(III) trajectory $\mathbf{p}_{T,I}$ results from an optimization minimizing travel time while respecting the lane boundaries.

The centerline (I) is selected because it is a self-evident choice by many human drivers; the rightmost lane (II), accounting for the regulation of driving at the very right, shows the influence of a lateral offset on the loads; and the time-optimal trajectory (III) is calculated because sporty test drivers tend to cut a corner, representing the 99% customer.

The entire surface of the customer route was measured in advance by an external supplier using optical methods [35]. After processing these data, information about the centerline $\mathbf{p}_{L,M}(s)$ of the road as well as the lane width $w_L(s)$ is available.

The definition of the centerline reference trajectory $\mathbf{p}_{T,M}(s) \equiv \mathbf{p}_{L,M}(s)$ is trivial, as the data points are already available from the measurement. The rightmost reference trajectory $\mathbf{p}_{T,R}$ furthest to the right while respecting the vehicle width w_V is given as

$$\begin{aligned}\mathbf{p}_{T,R} &= \begin{bmatrix} x_{T,R}(s) \\ y_{T,R}(s) \end{bmatrix} \\ &= \mathbf{p}_{L,M}(s) + \begin{bmatrix} sin\,\gamma \\ -cos\,\gamma \end{bmatrix} \cdot \frac{w_L(s) - w_V}{2} \quad \text{where} \quad \gamma(s) = \arctan\left(\frac{\mathrm{d}y_{L,M}}{\mathrm{d}x_{L,M}}\right) \quad . \end{aligned} \tag{16}$$

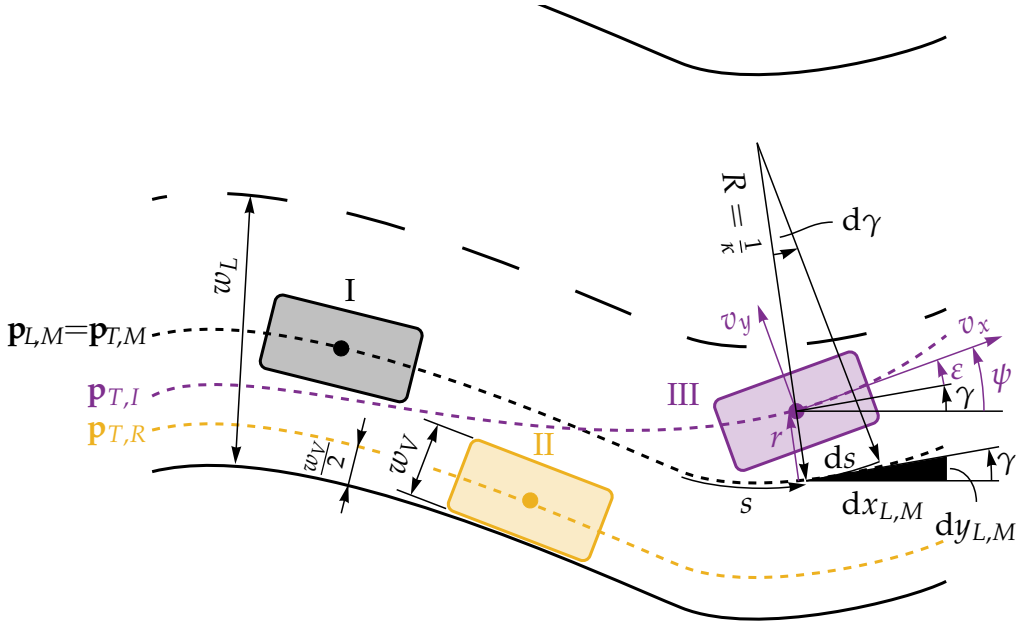


Figure 10. Measured road lane and possible vehicle reference trajectories for (I) middle (▬ ▬), (II) rightmost (▬ ▬) and (III) time-optimal path (▬ ▬), each inside lane boundaries represented by the road boundaries (▬) and lane separator (▬ ▬).

The calculation of reference trajectory $\mathbf{p}_{T,I}$ is significantly more challenging. To traverse a given route in minimal time, an optimal control problem (OCP) must be solved, where an already existing algorithm [30] is adapted. This algorithm is selected since the parameters of the associated vehicle model are adjustable to commonly available vehicle data without further measurements and due to the already implemented consideration of

vehicle limitations. The optimization goal is to reduce the travel time taking into account vehicle parameters, the route and the lane width. The optimization is constrained by vehicle kinematics and dynamics w.r.t. the road, which can be expressed by first-order differential equations

$$\dot{\mathbf{x}}(t) = \mathbf{f}(\mathbf{x}, \mathbf{u}) \tag{17}$$

relating the states

$$\mathbf{x} = \begin{bmatrix} v_x & v_y & \dot{\psi} & \omega_f & \omega_r & r & \varepsilon \end{bmatrix}^T \tag{18}$$

to controls

$$\mathbf{u} = \begin{bmatrix} M_f & M_r & \delta \end{bmatrix}^T \quad . \tag{19}$$

The state vector $\mathbf{x}$ includes the vehicle velocity state given by longitudinal and lateral center velocities v_x, v_y and yaw velocity $\dot{\psi}$. Additionally, the angular velocities of the front wheel ω_f and rear wheel ω_r are taken into account. Further, r and ε describe the deviation of the vehicle from the lane centerline and the yaw error; see Figure 10. To enable control of the vehicle solely by drive or braking torques M_f, M_r on the front and rear axle, respectively, as well as the steering angle δ, these quantities are summarized in the control vector $\mathbf{u}$.

For solving the optimization problem efficiently, the inertial vehicle position is transformed into the Frenet frame [36], which results in vehicle system equations expressed in terms of route parameters [37]. This comprises the coordinate s along the reference trajectory, the lateral deviation r from the lane centerline, and the heading error $\varepsilon = \psi - \gamma$ between the yaw angle ψ of the car and the course angle γ of the lane. Time derivatives are denoted as $\dot{\bullet} = \mathrm{d}\bullet/\mathrm{d}t$. Considering Figure 10, one can derive the relation

$$\mathrm{d}s = R\,\mathrm{d}\gamma \rightarrow \dot{s} = R\,\dot{\gamma} \rightarrow \dot{\gamma} = \kappa\,\dot{s} \quad . \tag{20}$$

The vehicle velocity along the road tangent can be obtained from projection as

$$v_x \cos\varepsilon - v_y \sin\varepsilon = (R - r)\,\dot{\gamma} \quad . \tag{21}$$

Inserting Equation (20) yields with $R = 1/\kappa$

$$\frac{\mathrm{d}}{\mathrm{d}t} s = \frac{v_x \cos\varepsilon - v_y \sin\varepsilon}{1 - r\,\kappa} \quad . \tag{22}$$

Projection of vehicle velocity components onto the normal road direction yields

$$\frac{\mathrm{d}}{\mathrm{d}t} r = v_x \sin\varepsilon + v_y \cos\varepsilon \quad . \tag{23}$$

Derivation of the heading error $\varepsilon = \psi - \gamma$ w.r.t. time and inserting quantities from Equations (20) and (22) yields

$$\frac{\mathrm{d}}{\mathrm{d}t}\varepsilon = \dot{\psi} - \kappa\frac{\mathrm{d}s}{\mathrm{d}t} = \dot{\psi} - \frac{\kappa}{1 - r\,\kappa}\left(v_x \cos\varepsilon - v_y \sin\varepsilon\right) \quad . \tag{24}$$

The remaining part of state Equation (17) is derived similarly to the work of Elbal [30], but instead of the double-track model, a simplified single-track model (Figure 11) is used, which is expanded by a Pacejka tire model, wheel inertia, longitudinal wheel load distribution and aerodynamic forces. The single-track model is sufficient for getting the time-optimal path, whereas later the determination of the chassis loads is based on the more realistic MBS model and overlayed control described in Section 2 involving all necessary car characteristics.

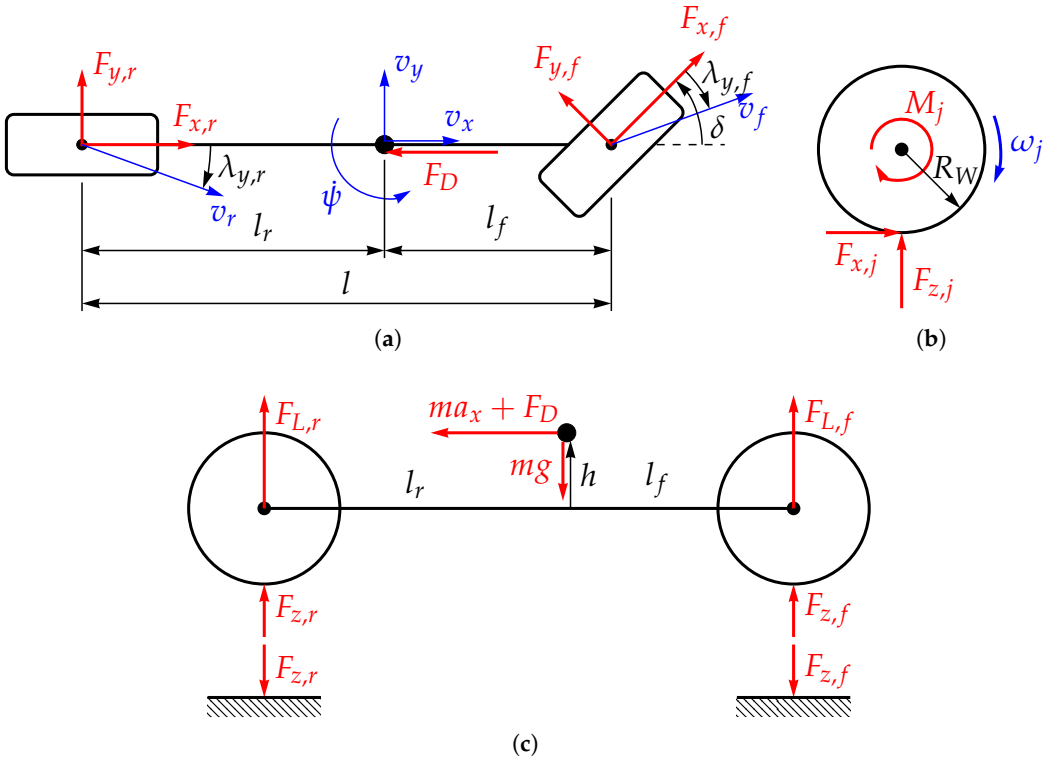


Figure 11. Single-track vehicle model (**a**), corresponding wheel forces (**b**) and side-view with forces acting on the vehicle (**c**).

Newton's and Euler's laws for the single-track model in Figure 11a with total mass m and moment of inertia $I_{V,z}$ yield

$$m\dot{v}_x = F_{x,r} + F_{x,f}\,\cos\delta - F_{y,f}\,\sin\delta - F_D \tag{25}$$

$$m\dot{v}_y = F_{y,r} + F_{x,f}\,\sin\delta + F_{y,f}\,\cos\delta \tag{26}$$

$$I_{V,z}\,\ddot{\psi} = l_f\,F_{x,f}\,\sin\delta + l_f\,F_{y,f}\,\cos\delta - l_r\,F_{y,r} \tag{27}$$

taking into account wheel contact forces and the aerodynamic drag force $F_D = (1/2)\,\varrho\,c_W\,A\,v_x^2$ [30], as higher speeds are expected for this OCP. The longitudinal front and rear wheel forces $F_{x,f}$ and $F_{x,r}$ result from control of the drive moments M_j taking into account the wheel radius R_W, wheel moments of inertia $I_{W,y}$ and angular speeds ω_j (c. f. Figure 11b):

$$I_{W,y}\,\dot{\omega}_j = M_j - F_{x,j}\,R_W \quad , j \in \{f, r\} \quad . \tag{28}$$

The wheel forces are computed with the tire model by Pacejka [22]. As the coefficients usually apply only for a single wheel, the resulting tire forces are doubled to get the forces per axle

$$F_{i,j} = 2 \cdot D_j\,\sin\{C_i\,\arctan[B_i\,\lambda_{i,j} - E_i(B_i\,\lambda_{i,j} - \arctan\,B_i\,\lambda_{i,j})]\}\ , \quad i \in \{x, y\},\ \ j \in \{f, r\}. \tag{29}$$

The longitudinal behavior ($i = x$) of a tire depends on its longitudinal slip

$$\lambda_{x,j} = \frac{\omega_j\,R_W - v_{x,j}}{v_{x,j}} \quad , \tag{30}$$

where $v_{x,r} = v_x$ and $v_{x,f} = v_x\,\cos\delta - (v_y + \dot{\psi}\,l_f)\,\sin\delta$. The lateral slip ($i = y$), also known as tire slip angle, of the front and rear axles is

$$\lambda_{y,f} = \delta - \arctan\left(\frac{\dot{\psi}\, l_f + v_y}{v_{x,f}}\right) \quad , \quad \lambda_{y,r} = \arctan\left(\frac{\dot{\psi}\, l_r - v_y}{v_{x,r}}\right) \quad . \tag{31}$$

While the stiffness factor B, the shape factor C and the curvature factor E in Equation (29) are constant and can be derived from measurements or alternative tire models, the peak value factor $D_j = \mu_j\, F_{z,j}^W$ [22] depends on the vertical wheel load

$$F_{z,f}^W = \frac{F_{z,f}}{2} = \frac{1}{2} \cdot \left(\frac{1}{l} \cdot \left(m\, g\, l_r - (m\, a_x + F_D)\, h\right) - F_{L,f}\right) \tag{32}$$

$$F_{z,r}^W = \frac{F_{z,r}}{2} = \frac{1}{2} \cdot \left(\frac{1}{l} \cdot \left(m\, g\, l_f + (m\, a_x + F_D)\, h\right) - F_{L,r}\right) \tag{33}$$

of a single wheel, respectively. The first formula, e.g., originates from moment equilibrium $\left(F_{L,f} + F_{z,f}\right) l - mgl_r + (ma_x + F_D)\, h = 0$ of the whole vehicle in Figure 11c after halving the result. Therefore, the dynamic load distribution caused by deceleration and acceleration is taken into account, where, for simplicity, vertical body movements are disregarded, whereas the front and rear lift forces $F_{L,j} = (1/2)\, \varrho\, c_{L,j}\, A\, v_x^2$, $j \in \{f, r\}$ [30], reducing the normal tire force, are considered. Further, a friction coefficient

$$\mu_j = \left(\mu_0 + p_{D2} \cdot \frac{F_{z,j} - F_{z0}}{F_{z0}}\right) \tag{34}$$

is incorporated, consisting of basic friction μ_0 and a load-dependent friction term depending on the deviation from the nominal load F_{z0}, scaled by a tire-specific factor p_{D2}.

The torques M_j, $j \in \{f, r\}$, acting on the front and rear axles are composed of braking torque $M_{B,j}$ and drive torque $M_{D,j}$, respectively: $M_j = M_{D,j} - M_{B,j}$. The brake torque M_B is distributed between the front and rear axles according to the brake torque distribution $k_B = M_{B,f}/M_{B,r}$, which is here chosen as $k_B = 2.3$ and implemented in the vehicle [38]. For an all-wheel drive, the total drive torque M_D is typically divided as 45:55 to front and rear axles, resulting in drive torque distribution $k_D = M_{D,r}/M_D = 0.55$. The imprinted moments on front and rear are thus [30]

$$M_f = (1 - k_D)\, M_D - \frac{k_B}{1 + k_B}\, M_B \quad , \quad M_r = k_D\, M_D - \frac{1}{1 + k_B}\, M_B \quad . \tag{35}$$

For consistency, Equation (17) should be transferred from the time domain to the path domain, since the traveled path s appears as an independent variable in the path description in Section 4. According to [30], this can be achieved by

$$\frac{\mathrm{d}}{\mathrm{d}s}\mathbf{x} = \frac{\mathrm{d}\mathbf{x}}{\mathrm{d}t} \cdot \frac{\mathrm{d}t}{\mathrm{d}s} =: \mathbf{f}(\mathbf{x}, \mathbf{u}) \cdot S_f \quad , \tag{36}$$

where $S_f = 1/\dot{s}$ may be computed from Equation (22). In explicit form, the state equation summarizes dynamics Equations (25)–(28) and kinematics Equations (23) and (24) resulting in

$$\frac{\mathrm{d}}{\mathrm{d}s}\mathbf{x} = \begin{bmatrix} \left(F_{x,r} + F_{x,f}\, \cos\delta - F_{y,f}\, \sin\delta - F_D\right)/m \\ \left(F_{y,r} + F_{x,f}\, \sin\delta + F_{y,f}\, \cos\delta\right)/m \\ \left(l_f\, F_{x,f}\, \sin\delta + l_f\, F_{y,f}\, \cos\delta - l_r\, F_{y,r}\right)/I_{V,z} \\ \left(M_f - F_{x,f}\, R_W\right)/I_{W,y} \\ \left(M_r - F_{x,r}\, R_W\right)/I_{W,y} \\ v_x\, \sin\varepsilon + v_y\, \cos\varepsilon \\ \dot{\psi} - \kappa/S_f \end{bmatrix} \cdot S_f \tag{37}$$

where

$$S_f = \frac{1 - r\,\kappa}{v_x\,\cos\varepsilon - v_y\,\sin\varepsilon}\,. \tag{38}$$

The time-optimal trajectory is obtained by solving an optimal control problem, where the objective is to minimize the total lap time [30]

$$t_{lap} = \int_0^{t_{lap}} \mathrm{d}t = \int_0^{s_{lap}} \frac{\mathrm{d}t}{\mathrm{d}s}\,\mathrm{d}s = \int_0^{s_{lap}} S_f\,\mathrm{d}s \tag{39}$$

subject to vehicle dynamics (c. f. Equation (37)), tire friction constraints, lane boundary constraints and actuator limitations:

$$\min_{\mathbf{u}} J(\mathbf{u}) = \min_{\mathbf{u}} \int_0^{s_{lap}} S_f(\mathbf{u})\,\mathrm{d}s \tag{40}$$

$$\text{s. t.} \qquad \frac{\mathrm{d}\mathbf{x}}{\mathrm{d}s} = \mathbf{f}(\mathbf{x},\mathbf{u}) \cdot S_f\,, \tag{41}$$

$$\frac{F_{x,j}^2 + F_{y,j}^2}{F_{z,j}^2} \leq \mu_j^2\,, \quad j \in \{f, r\}\,, \tag{42}$$

$$-\frac{w_L + w_V}{2} \leq r \leq \frac{w_L - w_V}{2}\,, \tag{43}$$

$$\mathbf{u}_{min} \leq \mathbf{u} \leq \mathbf{u}_{max} \quad . \tag{44}$$

Equation (44) restricts the steering angle δ, as well as torques M_f and M_r on the front and rear axles due to powertrain limitations. To prevent non-physical solutions, simultaneous application of driving and braking torque is prohibited by $M_D \cdot M_B = 0$. This constraint hinders the optimizer from exploiting the simplified brake torque distribution by counteracting braking torque with positive drive torque at another axle. Variation of S_f requires an unambiguous assignment of traveled distance and time guaranteed by $v_x > 0\ \forall s$.

The optimization problem (40)–(44) is described using CasADi [39]. This open-source computer algebra system, which enables the symbolic representation of the above equations, was originally designed for automatic differentiation. CasADi offers an interface for various solvers such as the optimization algorithm IPOPT [40]. This Interior Point OPTimizer is a gradient-based optimization method for nonlinear constrained optimization problems using an interior-point method and Newton-based search directions together with a filter line-search strategy. The solver uses the orthogonal collocation method, transforming the continuous optimal control problem into a sparse nonlinear programming problem using Legendre collocation points and polynomials for steering wheel angle $\delta(s)$ and wheel torques $M_f(s)$, $M_r(s)$, which determine optimization parameter $\mathbf{u}$. The time-optimal trajectory $\mathbf{p}_{T,I}(s)$ emerges implicitly from the optimization as the optimal lateral displacement $r(s)$ along the track.

In order to validate the time-optimal trajectory found by the above approach, a generic route with constant width is specified. Based on the curvature of the centerline shown in Figure 12b, the S-curve in Figure 12a is obtained. In reference to real road construction, clothoids with linear curvature increase/decrease between different radii are chosen [34].

Application of the above optimization algorithm yields the trajectory shown in Figure 13. The trajectory along the centerline results in a travel time of 11.13 s, whereas the time-optimal solution reduces it to 10.23 s. The ideal line demonstrates the typical motion known from motorsport: it starts on the outside of the first curve, passes the apex of the curves closest to the inside edges and then exits the second curve on the outside.

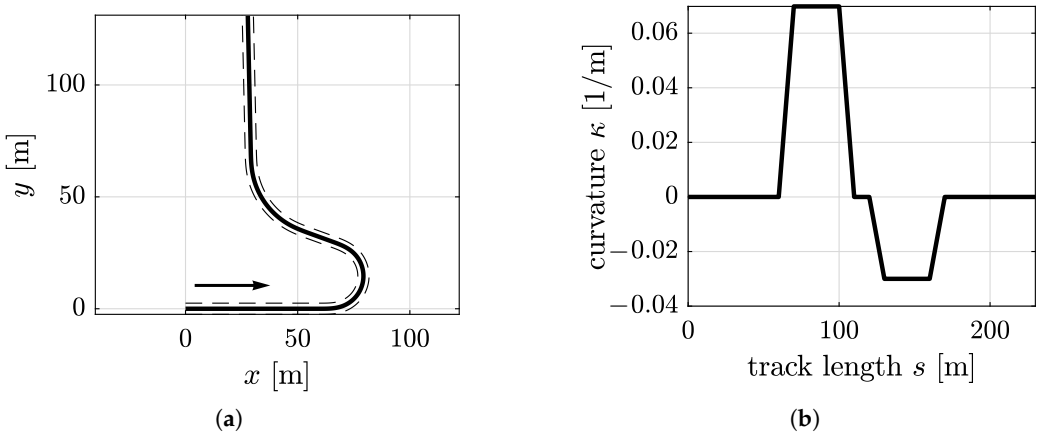


Figure 12. Generic track of S-shaped curve with lane boundaries (▬ ▬) (**a**) and curvature (**b**) for validating the minimal lap time algorithm.

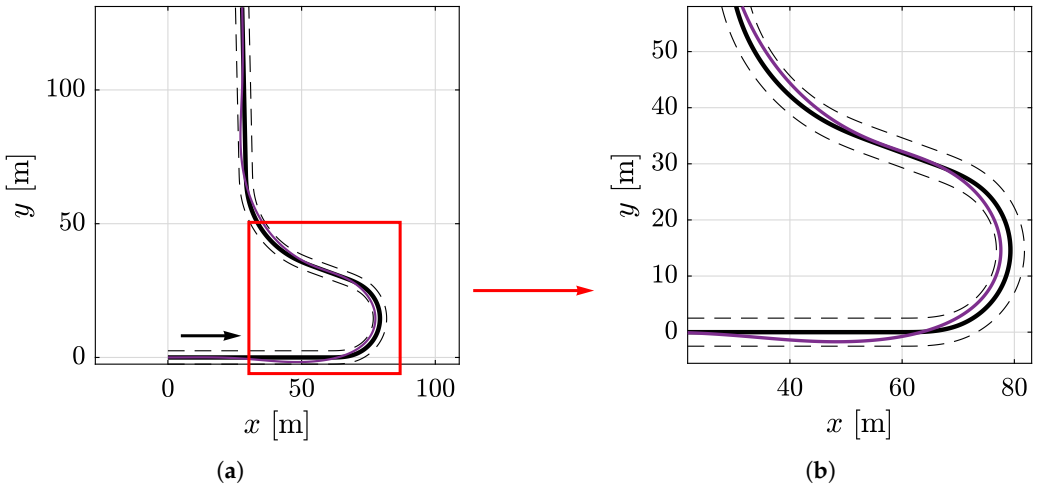


Figure 13. Centerline (▬) and time-optimal (▬) trajectory for S-shaped curve (**a**) within lane boundaries (▬ ▬) with detailed view (**b**).

5. Comparison of Chassis Loads

This section consolidates all findings and results of the previous parts of the paper. The vehicle, modeled in Simpack according to Section 2, travels along the three paths, including the time-optimal trajectory found by the algorithm in Section 4, with the velocity profile constrained by curvature as introduced in Section 3. The first application uses the generic example of the S-curve in Figure 12. The corresponding curvature courses shown in Figure 14a and a maximum speed of 80 km/h = 22.22 m/s result in the generic speed profiles in Figure 14b, where the admissible lateral and longitudinal accelerations for braking and driving are chosen as $\hat{a}_y = 4\,\mathrm{m/s^2}$, $\hat{a}_B = 5\,\mathrm{m/s^2}$, $\hat{a}_D = 3\,\mathrm{m/s^2}$, respectively. It can be seen that in the first turn the curvature is too high, reducing the velocity for all three trajectories. Due to the smaller curvature in the second turn, the necessary speed reduction is less pronounced. The reason for the occurrence of curvature ramps at different track locations in Figure 14b is that the changed curvature results in different track lengths.

Simulation of the MBS-model, while the Simpack Driver maintains the track and velocity in Figure 14, yields the chassis loads shown in Figure 15. To simplify comparison of loads, they are plotted over track length s instead of time. For ease of understanding, wheel hub forces are shown, but in principle also structural forces of the suspension could be deduced from the simulation.

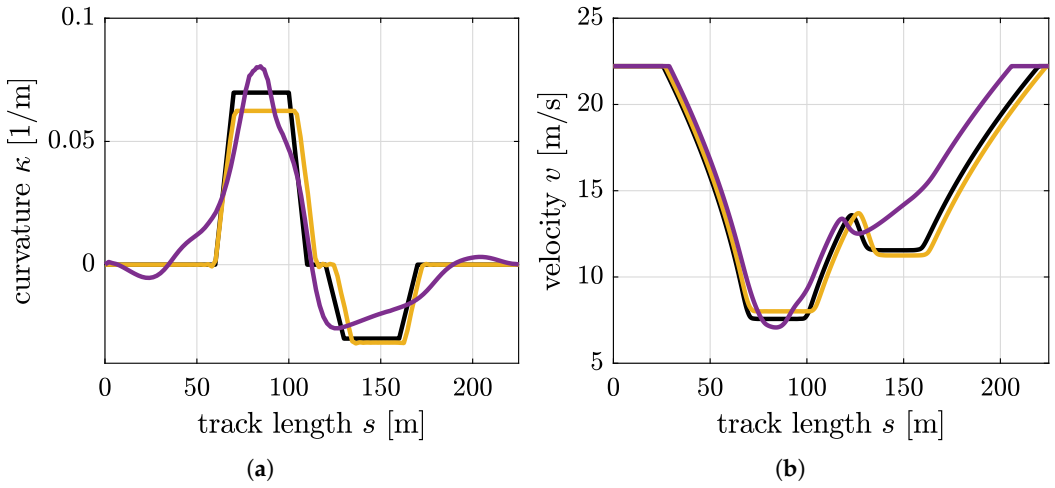


Figure 14. Curvatures (**a**) and velocity profiles (**b**) for motions along centerline (—), rightmost path (—) and time-optimal path (—) of S-shaped road, respectively.

Figures 15a,c show the longitudinal and lateral hub forces of the front left wheel, respectively. As the time-optimal trajectory allows passing turns at higher speed, the driver does not need to brake as hard as for the mean or rightmost trajectory, resulting in lower braking forces in Figure 15a. The lower these forces are, the lower are the chassis loads determining the endurance of components.

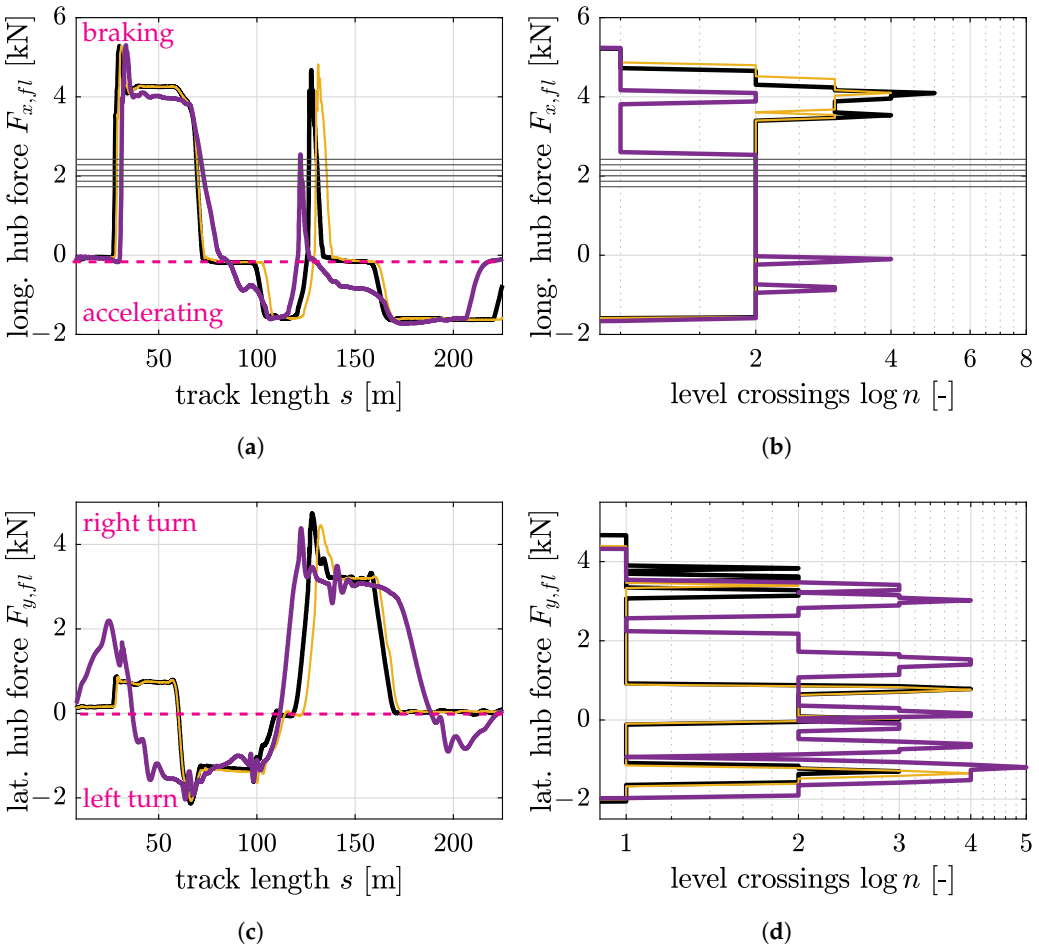


Figure 15. Longitudinal load acting on the front left wheel hub along the traveled distance (**a**) and corresponding level crossings (**b**) as well as the lateral load (**c**) and level crossings (**d**) for centerline (—), rightmost path (—) and time-optimal path (—) along S-shaped lane, respectively.

As time series become longer with increasing track length and consequently harder to analyze; the typical counting of level crossings is introduced [14]. Figure 15b shows the number of level crossings corresponding to the time series in Figure 15a for $F_{x,fl}$. Generally spoken, the figure shows how often a dedicated force level is crossed. Levels are determined by dividing the obtained load range $[-1.7\,\mathrm{kN}, 5.3\,\mathrm{kN}]$ in 100 classes as indicated exemplary by black level lines in Figure 15a about 2 kN. If a class is fully passed in the positive direction, it is counted as one level crossing. The abscissa of Figure 15b shows the accumulated level crossings for specific loads represented by the ordinate. In terms of fatigue, this gives a very first assessment of load cycles acting on the chassis: with lower loads and fewer level crossings, the chassis components are stressed less. Regarding the lateral forces in Figure 15c,d, except for the first positioning of the model at $s \approx 20\,\mathrm{m}$, the peak values of all trajectories are at the same level because they are mostly limited by the admissible lateral acceleration $\hat{a}_y$ determining the lateral force $F_y \approx m\,\hat{a}_y$ regardless of curvature κ and speed v. Accordingly, the lateral loads for the vehicle remain the same for different trajectories/curvatures. A notable feature in Figure 15c is the constant lateral force of 0.6 kN starting at $s = 20\,\mathrm{m}$, where braking for the upcoming curve causes a lateral force due to the wheel toe-in.

Findings from the generic S-curve are now applied to a real road, which is a section extracted from the country road (see dashed box in Figure 1). While Figure 16a shows the course of the lane's centerline, the corresponding curvatures for the three trajectories middle, rightmost and time-optimal are shown in Figure 16b. The track starts with turns of moderate curvature and has one hairpin turn near the end, providing quite a representative mixture of different curvatures and velocities for a typical country road.

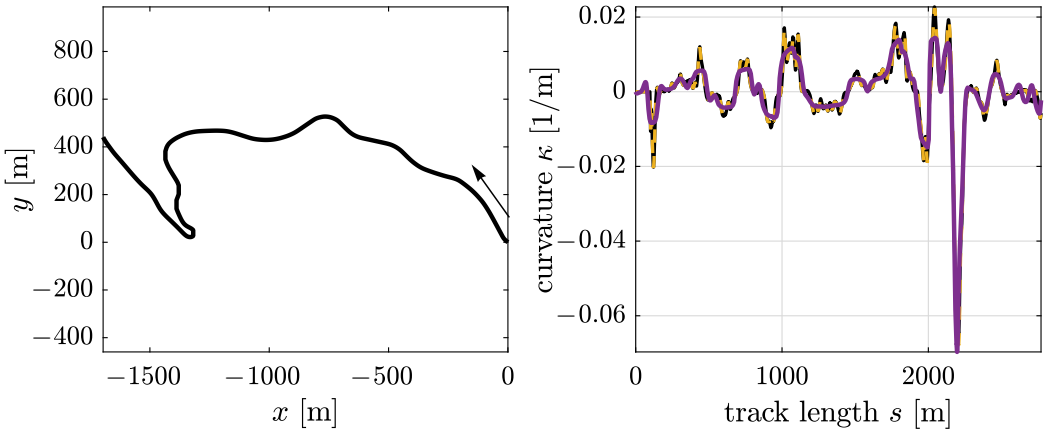


Figure 16. Considered piece of the country road (**a**), where an arrow indicates travel direction, and corresponding curvatures (**b**) of trajectories along centerline (—), rightmost lane (– –) and time-optimal path (—)

In Figure 17a,b, the longitudinal braking forces (positive values of $F_{x,fl}$) are surprisingly lower when following the time-optimal path (see, e.g., dashed boxes in Figure 17a) compared with the two other trajectories since typically one would expect higher loads for sporty driving. However, the result is explainable by fewer hard braking events required for the time-optimal lane, which either avoids braking ahead of curves or requires less deceleration, and thus results in lower longitudinal forces. A similar pattern is observed for negative longitudinal forces (acceleration), although not as pronounced. However, the lateral loads in Figure 17c,d differ only slightly between the three types of trajectories, where in particular the two profiles for centerline and rightmost paths are almost identical.

The maximum loads are somewhat lower for the time-optimal path, which is expected as already pointed out for the lateral force along the S-shaped curve. As the velocity profile is computed identically for all trajectories, most differences arise from variations in curvature and the associated braking and acceleration behavior before and after the corner.

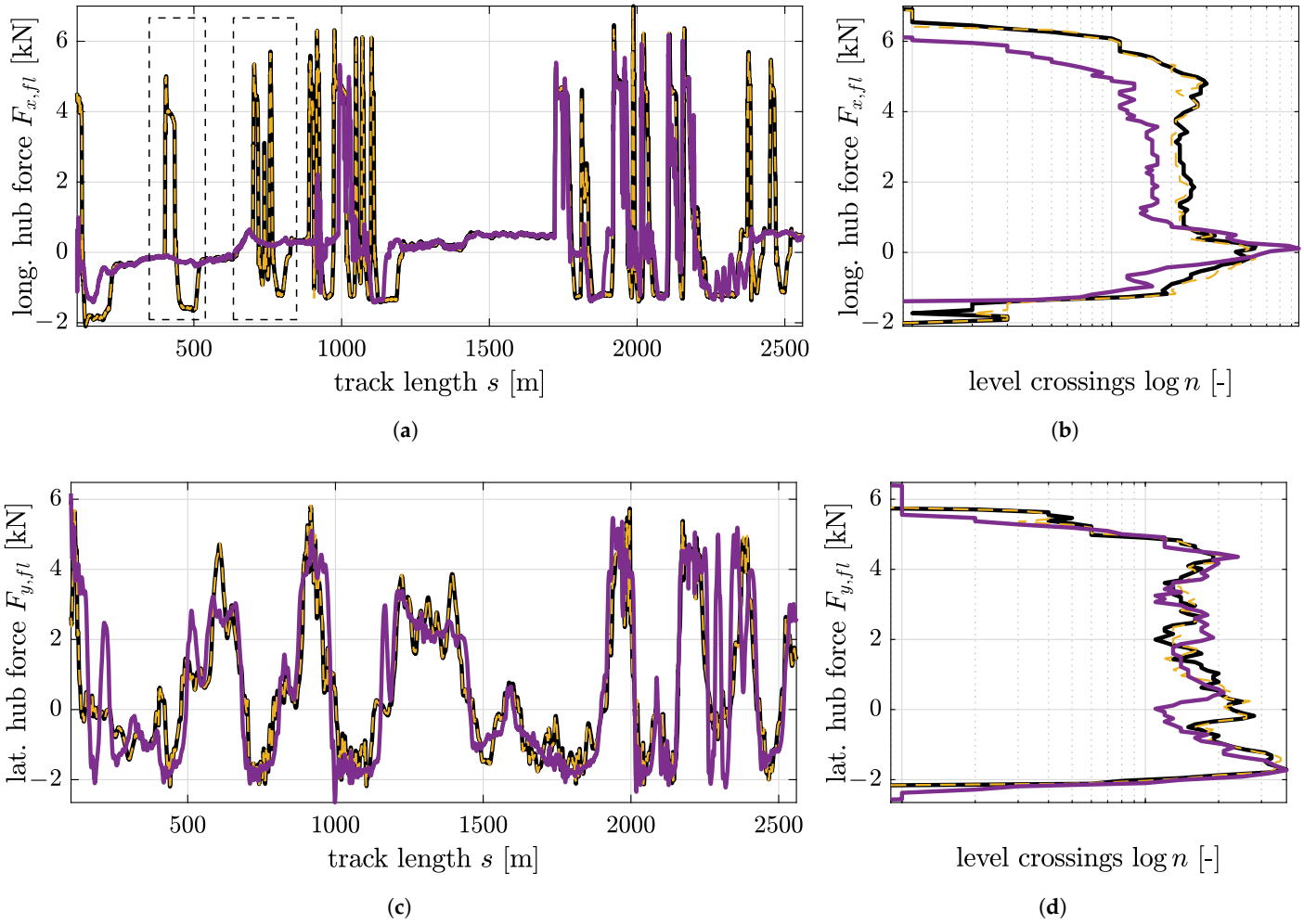


Figure 17. Country road: longitudinal load over traveled distance (**a**) and corresponding level crossings (**b**), as well as lateral load (**c**) and associated level crossings (**d**) for centerline (—), rightmost trajectory (– –) and time-optimal path (—), respectively.

6. Conclusions

To test functional components, primarily rubber bearings in car suspensions, a customer-oriented load profile is required, which has to be defined in such a way that the frequencies and amplitudes of the simulated signal later match the loads in the field as closely as possible. The investigations show that simulation based on a full-vehicle multibody system combined with a driver controller is able to keep the model on a predefined trajectory with a given speed, which avoids the need for physically existing prototypes and allows making important concept decisions in early phases of the development process.

The proposed concept allows defining a realistic speed profile according to legally permissible speed limits and restrictions imposed by road curvature, where limiting velocity ramps for acceleration and braking are used to soften hard transitions between suddenly changing speed levels. The investigation reveals that the speed profile depends on the chosen lateral motion, where three different reference trajectories are defined: centerline, rightmost trajectory and time-optimal path. Applications to a generic road and a public

country road used by Mercedes-Benz demonstrate that the choice of the trajectory has a significant influence on the calculated longitudinal loads. While the centerline and rightmost lane result in comparable loads, loads for the time-optimal path are significantly lower. Thus, this work gives a valuable insight into the impact of different trajectories combined with a corresponding speed profile on chassis loads. Further investigations covering uncertainties of driver behavior and comparisons with real-world test drivers and measured loads have to show which of the trajectories should ultimately be chosen for load calculation of functional components.

Author Contributions: Methodology and paper writing, M.B. and D.B.; software and investigation, M.B.; supervision, D.B. All authors have read and agreed to the published version of the manuscript.

Funding: This research received no external funding.

Data Availability Statement: The datasets presented in this article are not available due to privacy restrictions of the OEM. Requests to access the datasets should be directed to the corresponding author.

Conflicts of Interest: The authors declare no conflicts of interest.

References

1. Braess, H.-H.; Seiffert, U. *Vieweg Handbuch Kraftfahrzeugtechnik*; Springer: Wiesbaden, Germany, 2013.
2. Bundesministerium der Justiz und für Verbraucherschutz. Gesetz über die Neuordnung des Geräte- und Produktsicherheitsrechts (ProdSG). *Bundesgesetzblatt* **2011**, *57*, 2178–2208.
3. Köhler, M.; Jenne, S.; Pötter, K.; Zenner, H. *Zählverfahren und Lastannahme in der Betriebsfestigkeit*; Springer: Berlin/Heidelberg, Germany, 2012.
4. Jambhale, M.S.; Manel, V.A.; Kale, J.G.; Saraf, M.R. Vehicle Response and Real World Driving Pattern for Indian Scenario for Vehicle Development and Optimization Program. In Proceedings of the Symposium on International Automotive Technology, Pune, India, 9–12 January 2013.
5. Kumar, P.P.; Prakaash, J.; Kumar, P. Optimization of Proving Ground Durability Test Sequence Based on Relative Damage Spectrum. In Proceedings of the WCX World Congress Experience, Detroit, Michigan, USA, 10–12 April 2018.
6. Coura, I.; Maduro, F.; Passos, F.; Braga, M. Customer Profile Identification and Correlation Between the Customer Damage and Durability Tests. In Proceedings of the SAE BRASIL International Congress and Exhibit, Sao Paulo, Brazil, 14–18 October 2019.
7. Pötter, K.; Till, R.; Horst, M. Auslegungs- und Absicherungskonzepte der Betriebsfestigkeit—Potentiale und Risiken. In Proceedings of the Tagung des DVM-Arbeitskreises Betriebsfestigkeit 37, Munich, Germany, 6–7 October 2010; pp. 1–8.
8. Qian, B.; Hinkelmann, K.; Mauch, H.; Esderts, A. Ermittlung von Fahrwerkslasten aus CAN-Daten. In Proceedings of the Tagung des DVM-Arbeitskreises Betriebsfestigkeit 45, Stuttgart/Renningen, Germany, 26–27 September 2018; pp. 153–168.
9. Balakrishnan, S.; PP, A.; Kharul, R.; C, S. Accurate Estimation of Time Histories for Improved Durability Prediction Using Artificial Neural Networks. In Proceedings of the SAE World Congress & Exhibition, Detroit, MI, USA, 24–26 April 2012.
10. Gorges, C. *Identifying Customer Usage Profiles of Two-Wheeled Vehicles, Dissertation*; TU Berlin: Berlin, Germany, 2018.
11. Sonsino, C.M. Betriebsfestigkeit—Eine Einführung in die Begriffe und ausgewählte Bemessungsgrundlagen. *MP Mater. Test.* **2008**, *50*, 77–90.
12. Sonsino, C.M. Versuchszeitverkürzung in der Betriebsfestigkeitsprüfung: Methoden und Kompromisse. *MP Mater. Test.* **2003**, *45*, 133–144.
13. Alshuth, T.; Abraham, F.; Jerrmas, S. Parameter Dependence and Prediction of Fatigue Properties of Elastomere Products. *Rubber Chem. Technol.* **2002**, *75*, 635–642.
14. Haibach, E. *Betriebsfestigkeit: Verfahren und Daten zur Bauteilberechnung*; Springer: Berlin/Heidelberg, Germany, 2006.
15. Duni, E.; Toniato, G.; Saponaro, R.; Smeriglio, P.; Puleo, V. Vehicle Dynamic Solution Based on Finite Element Tire/Road Interaction Implemented through Implicit/Explicit Sequential and Co-Simulation Approach. In Proceedings of the SAE World Congress & Exhibition, Detroit, MI, USA, 13–15 April 2010.
16. Hu, H.; Zhong, Z. Explicit–Implicit Co-Simulation Techniques for Dynamic Responses of a Passenger Car on Arbitrary Road Surfaces. *Engineering* **2019**, *5*, 1171–1178.
17. Lieven, W.; Warnecke, U.; Schick, A.; Le-The, H. Festigkeits- und Betriebsfestigkeitsanalyse von PKW-Karosserien auf Basis virtuell ermittelter Betriebsbelastungen. In Proceedings of the Tagung des DVM-Arbeitskreises Betriebsfestigkeit 33, Steyr, Austria, 11–12 October 2006; pp. 177–188.

18. Schmeitz, A.; Versteden, W.; Eguchi, T. Road Load Simulation using the MF-Swift Tire and OpenCRG Road Model. In Proceedings of the SAE 2011 World Congress & Exhibition, Detroit, MI, USA, 12–14 April 2011; SAE Technical Paper 2011-01-0190.
19. Weber, T. Betriebslasten in der Fahrzeugentwicklung—Simulation Gesamtfahrzeug. In Proceedings of the Tagung des DVM-Arbeitskreises Betriebsfestigkeit 41, Ingolstadt, Germany, 8–9 October 2014; pp. 115–128.
20. Pawar, P.; Joshi, O.; Saraf, M. Generation of 3D-Digital Indian Public Road Profile Database and Its Application for Vehicle Development through Road-Vehicle Interaction Study. *SAE Int. J. Veh. Dyn. Stability, NVH* **2017**, *1*, 80–88.
21. Brandes, S. *Gesamtfahrzeugsimulation betriebsfestigkeitsrelevanter Manöver unter Berücksichtigung von Fahrwerkregelsystemen, Dissertation*; TU Darmstadt: Darmstadt, Germany, 2016.
22. Pacejka, H.P. *Tire and Vehicle Dynamics*; Elsevier: Amsterdam, The Netherlands, 2012.
23. Bösch, P. *Der Fahrer als Regler, Dissertation*; TU Wien: Wien, Austria, 1991.
24. Wang, W.; Xi, J.; Chen, H. Modeling and Recognizing Driver Behavior Based on Driving Data: A Survey. *Math. Probl. Eng.* **2014**, *2014*, 245641.
25. Dassault Systems SIMULIA User Assistance 2022x.5. *User Manual and Documentation, Integrated into the Software*; Dassault Systèmes: Vélizy-Villacoublay, France, 2022.
26. Massaro, M.; Limebeer, D.J.N. Minimum-lap-time Optimisation and Simulation. *Veh. Syst. Dyn.* **2021**, *59*, 1069–1113.
27. González, D.; Pérez, J.; Milanés, V.; Nashashibi, F. A Review of Motion Planning Techniques for Automated Vehicles. *IEEE Trans. Intell. Transp. Syst.* **2015**, *17*, 1135–1145.
28. Li, J.; Li, S.; Wang, J. Trajectory Planning for Lane Change with Intelligent Vehicles Using Fuzzy Logic and a Dynamic Programming and Quadratic Programming Algorithm. *Electronics* **2024**, *13*, 4732.
29. He, Y.; Wu, J.; Xu, F.; Liu, X.; Wang, S.; Cui, G. Path Tracking Control Based on T-S Fuzzy Model for Autonomous Vehicles with Yaw Angle and Heading Angle. *Machines* **2024**, *12*, 375.
30. Jiménez Elbal, A.; Zarzuelo Conde, A.Z.; Siampis, E. Trajectory Optimisation - A Simultaneous Approach to the Minimum Lap Time Problem. *World Electr. Veh. J.* **2024**, *8*, 366—392.
31. Schiehlen, W.; Eberhard, P. *Technische Dynamik*; Springer: Wiesbaden, Germany, 2020.
32. Ress, C.; Balzer, D.; Bracht, A.; Löwenau, J. Adasis Protocol for Advanced In-vehicle Applications. In Proceedings of the ITS World Congress 15, New York City, NY, USA, 16–20 November 2008; pp. 16–20.
33. Pandazis, J.; Schucht, A.; Wandt, C.; Pradarutti, B.; Reiter, M.; van den Berg, R. *ADASIS White Paper: Advanced Driver Assistance Systems Interface Specifications*; ADASIS: Brussels, Belgium, 2024.
34. Richter, T. *Road Planning—Freeways and Country Roads*; Springer: Wiesbaden, Germany, 2023.
35. Haigermoser, A.; Luber, B.; Rauh, J.; Gräfe, G. Road and Track Irregularities: Measurement, Assessment and Simulation. *Veh. Syst. Dyn.* **2015**, *53*, 878–957.
36. Perantoni, G.; Limebeer, D.J.N. Optimal Control for a Formula One Car with Variable Parameters. *Veh. Syst. Dyn.* **2014**, *52*, 653—678.
37. Reiter, R.; Diehl, M. Parameterization Approach of the Frenet Transformation for Model Predictive Control of Autonomous Vehicles. In Proceedings of the European Control Conference, Virtual, 29 June–2 July 2021; pp. 2414—2419.
38. Veneri, M.; Massaro, M. A Free-trajectory Quasi-steady-state Optimal-control Method for Minimum Lap-time of Race Vehicles. *Veh. Syst. Dyn.* **2020**, *58*, 933–954.
39. Andersson, J.A.E.; Gillis, J.; Horn, G.; Rawlings, J.B.; Diehl, M. CasADi—A Software Framework for Nonlinear Optimization and Optimal Control. *Math. Program. Comput.* **2019**, *10*, 1–36.
40. Wächter, A.; Biegler, L.T. On the Implementation of an Interior-point Filter Line-search Algorithm for Large-scale Nonlinear Programming. *Math. Program.* **2006**, *106*, 25–57.

Disclaimer/Publisher's Note: The statements, opinions and data contained in all publications are solely those of the individual author(s) and contributor(s) and not of MDPI and/or the editor(s). MDPI and/or the editor(s) disclaim responsibility for any injury to people or property resulting from any ideas, methods, instructions or products referred to in the content.